IEEE Open Journal of
Power Electronics

Received 25 February 2024; revised 14 April 2024; accepted 26 April 2024. Date of publication 2 May 2024;
date of current version 9 May 2024. The review of this article was arranged by Associate Editor Youngjong Ko.

Digital Object Identifier 10.1109/OJPEL.2024.3395293

Current-Fed Dual Active Bridge Converter With Asymmetric Three-Phase Transformer

YIYU CHEN [1] (Student Member, IEEE), RYOSUKE OTA [2] (Member, IEEE), AND NOBUKAZU HOSHI [1] (Senior Member, IEEE)

[1]Department of Electrical Engineering, Tokyo University of Science, Chiba 278-8510, Japan
[2]Faculty of Systems Design, Department of Electrical Engineering and Computer Science, Tokyo Metropolitan University, Hino Tokyo 191-0065, Japan

CORRESPONDING AUTHOR: YIYU CHEN (e-mail: 7322564@ed.tus.ac.jp)

ABSTRACT This paper proposes a current-fed dual active bridge (DAB) converter with an asymmetric three-phase transformer, aiming to achieve high efficiency over a wide operating range. In the proposed converter, the neutral point (junction) of the three-phase transformer is clamped by the DC power supply on the primary side and by a capacitor on the secondary side, decoupling each phase of the transformer. This configuration enables transformers with different turn ratios, allowing for the selection of energizing phases according to the circuit condition. In order to show the effectiveness of the proposed converter, this paper models the power losses of the proposed converter and shows its efficiency characteristics through theoretical analysis. Furthermore, the efficient operating modes corresponding to the circuit and load conditions are indicated based on the theoretical analysis. Experiments using a 1 kW prototype demonstrate the validity of the theoretical analysis. Consequently, the efficiency characteristics obtained experimentally indicate similar trends from the theoretical analysis, confirming that the proposed converter operates efficiently over a wide range. Additionally, the proposed converter is compared using the analytical models to a DAB converter with a symmetric three-phase transformer. As a result, it is shown that the proposed converter can achieve an efficiency improvement of more than five percentage points (% points) under light loads, and the efficiency drop in specific operating points can be capped by 1.25% points.

INDEX TERMS Isolated DC–DC converter, dual active bridge converter, asymmetric three-phase transformer, zero voltage switching.

I. INTRODUCTION

Lithium-ion batteries (LiBs) can be used as storage batteries in portable power systems. In this case, a DC–DC converter, which boosts the DC voltage, and an inverter are integrated into the power system. The DC–DC converter needs to have an isolated input-output, bidirectional power conversion capability, and the ability to operate over a wide range of input-output voltage ratios and load conditions. Additionally, high power conversion efficiency is desired from the perspective of energy efficiency, miniaturization, and weight reduction.

A converter that can meet these requirements is the dual active bridge (DAB) converter. In the DAB converter, at medium loads and in operating regions where the input-output DC voltage ratio is close to the transformer's turn ratios, it can operate with a high power factor and enable zero voltage switching (ZVS), leading to a high efficiency [1], [2]. However, in other operating ranges, the efficiency significantly decreases due to an increase in reactive current caused by the low power factor and hard-switching operation.

Approaches to address these challenges can be broadly categorized into those from a control perspective and those from a circuit-topology perspective. One of the methods to approach control involves controlling the phase-shift angle between legs in the primary and secondary DC–AC converter (active bridge), in addition to the phase-shift control between the active bridges [3], [4], [5], [6], [7], [8], [9], [10], [11], [12]. In addition, there are also methods for high efficiency under light loads, including discontinuous current modes [13], [14], and intermittent operation [15].

Regarding the circuit-topology approach, methods include employing a DC–AC converter that can switch the voltage applied to the transformer [16], [17], [18], [19], [20], [21].

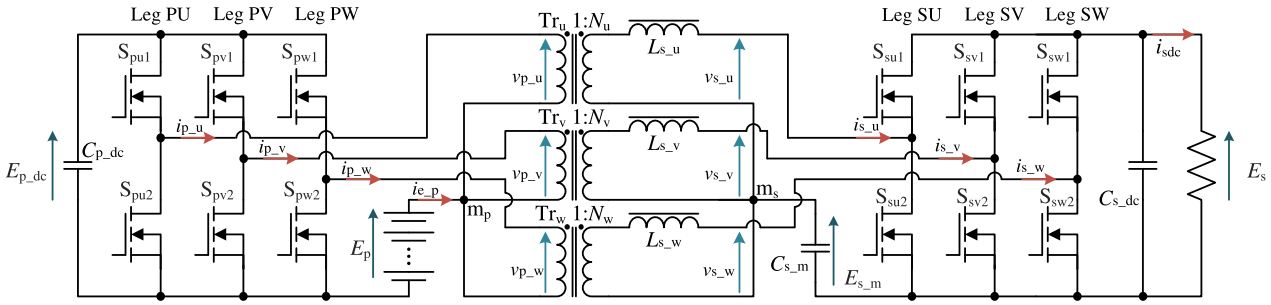

FIGURE 1. Proposed current-fed DAB converter with the asymmetric three-phase transformer.

There is also a method that can switch between energized transformers or windings [22], [23]. By using multilevel techniques [16], [17], [18], [19], [20] or DC blocking capacitors [21] for an active bridge, the voltage applied to the transformer can be switched, improving the controllability of the current. However, the benefits of multilevel converters are difficult to obtain when utilizing a low-voltage portable battery as a power source for consumer electronics. Additionally, there is concern regarding increased conduction losses due to the increase in the number of series-connected power devices.

On the other hand, the literature [22] proposes a DAB converter using three vertically connected arms and two transformers. This converter topology can connect the two transformers in series or parallel depending on the input–output voltage ratio and load, achieving high efficiency across a wide operating range. However, a problem is an increase in conduction losses due to the series-connection of power devices.

Furthermore, the literature [23] allows the change of the turn ratios of the transformer by employing a tap-changing transformer. This enables winding switching without an increase in magnetic components. However, using mechanical switches to change the turn ratios can lead to high cost, low reliability, and chattering issues during switching.

Efficiency improvement methods for three-phase DAB converters have been discussed as well as single-phase DAB converters [24], [25]. Although the efficiency is definitely enhanced, these strategies involve complex control. Furthermore, approaches with control methods generally have limitations in improving efficiency due to the circuit topology. In particular, the range of efficiency improvement regarding the input-output voltage ratio is strongly influenced by the turn ratio of the transformer, as mentioned earlier.

Thus, this paper proposes a current-fed DAB converter using an asymmetrical three-phase transformer, as shown in Fig. 1, aiming to expand the high-efficiency operating range relative to the voltage ratio and output power. In the proposed converter, the junction (neutral points) of the three-phase transformers are clamped by LiB (DC voltage supply) on the primary side and by a capacitor on the secondary side. Hence, each phase in the proposed converter is decoupled. Depending on the input–output voltage ratio and load, the proposed converter can select the energizing transformers and the number of phases. Essentially, this circuit configuration can be viewed as dual half-bridge (DHB) converters [26] running in three parallel.

With this configuration, while the efficiency maximum efficiency point in a three-phase operation can be slightly inferior to that of a conventional three-phase DAB converter with a symmetric turn ratios, efficient operations over a wide range can be expected. This makes it apt for applications such as portable power systems, where input–output voltage ratios and loads vary significantly.

The paper is organized as follows: Section II presents the configuration of the proposed converter and describes its typical operating modes. Section III models the power losses of the transformers and power devices in the converter. Furthermore, it clarifies the power loss and efficiency characteristics of the proposed converter and provides guidelines for selecting highly efficient operating modes. Section IV builds a 1 kW prototype to demonstrate the efficacy of the proposed converter and confirms the validity of the theoretical analysis by experiments. In Section V, the efficiency characteristics of a three-phase DAB converter with symmetric turn ratios are demonstrated utilizing the theoretical analysis models of Section III. The features of the proposed converter are highlighted by comparing the proposed converter and the three-phase DAB converter. Finally, conclusions are shown in Section VI.

II. OPERATION OF THE PROPOSED CONVERTER

In this chapter, the configuration of the proposed converter is first described. Then, the six operating modes of the proposed converter are shown and explained. Finally, a design guideline for the transformer and inductors in the proposed converter is presented.

A. CONFIGURATION OF THE PROPOSED CONVERTER

As shown in Fig. 1, the proposed converter comprises a three-phase current-fed DC/AC converter (active bridge) on the source side (primary side), a three-phase active bridge on the load side (secondary side), a three-phase transformer with different turn ratios for each phase, series inductors for power adjustment, and a clamp capacitor. Between the junction m_p of the primary side three-phase windings and the source of the lower switches, a LiB (power source) is connected. In

TABLE 1. Guideline for the Efficient Operation of the Proposed Converter

DC Voltage ratio E_s/E_p	Load		
	Light	Middle	Heavy
High	Mode W	Mode VW	Mode UVW
Middle	Mode V		
Low	Mode U	Mode UV	

addition, between the junction m_s of the secondary side three-phase windings and the source of the lower switches, a clamp capacitor C_{s_m} [F] is connected. The LiB and clamp capacitor C_{s_m} work as constant voltage sources and decouples each phase of the three-phase transformer.

Therefore, the proposed converter can operate each phase independently. Furthermore, the proposed converter can select the energizing phases and determine the number of energizing transformers according to the voltage ratio and the load. These operating modes can be classified into six, as shown in Table 1. Mode U is an operating mode that energizes a single-phase of the transformer with a turn ratios $N_u = n_{s\_u}/n_{p\_u}$, Mode V is an operating mode that combines a single-phase of the transformer with a turn ratios $N_v = n_{s\_v}/n_{p\_v}$, and Mode W is an operating mode that combines a single-phase of the transformer with a turn ratios $N_w = n_{s\_w}/n_{p\_w}$. Additionally, Mode UV is an operating mode that combines Mode U and Mode V in parallel, and Mode VW is an operating mode that combines Mode V and Mode W in parallel, suitable for medium load operations. Mode UVW is suitable for heavy load operations by energizing all three phases.

Generally, DAB converters operate efficiently in the operating range of medium load when the turn ratios of the transformer is equal to the input-output voltage ratio. Therefore, the three-phase transformer comprises three single-phase transformers with different turn ratios; transformers with different turn ratios are connected, and the energized phase is selected according to the DC voltage ratio E_s/E_p of the primary and secondary sides. Moreover a high-efficiency operation is realized by controlling the number of controlling phases according to the load. The details of these operations are described in the next chapter.

B. OPERATION OF THE PROPOSED CONVERTER

This chapter initially explains the operation of a single-phase of the proposed converter, using Mode V as an example. Subsequently, Mode UV and Mode UVW are described based on the operation of Mode V.

1) MODE V

Fig. 2 shows the operating waveforms during Mode V. In the three-phase active bridges on both the primary and secondary sides, only one leg, in each side, Leg PV and Leg SV, respectively, is operated during Mode V. The remaining

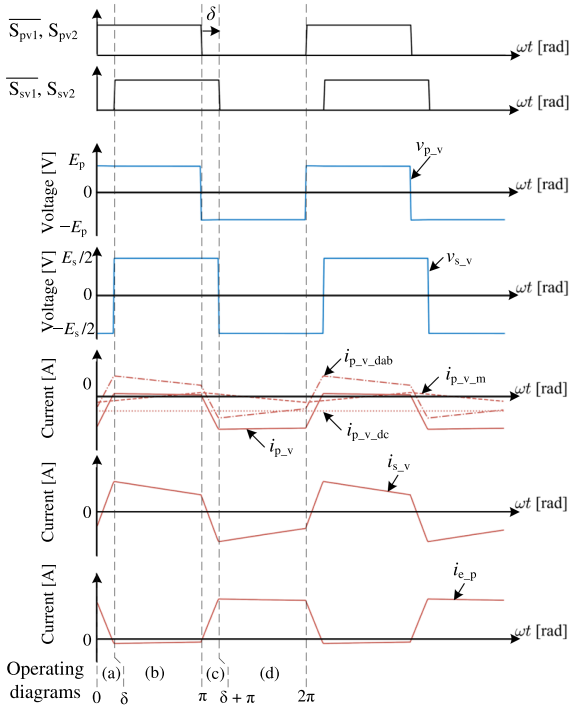

FIGURE 2. Operating waveforms of the proposed converter during Mode V.

legs are halted by off-signals. This mode, energizing only a single-phase, is used during light-load conditions.

Focusing on the primary side of phase-V, which comprises Leg PV and the primary winding of the transformer Tr_v, the configuration can be considered as a bidirectional chopper. From the perspective of the DC voltage supply, the primary winding of the transformer also functions as an inductor for a boost operation. A higher DC link voltage E_{p_dc} [V] is generated relative to the source voltage E_p [V]. The voltage E_{p_dc} can be expressed using E_p and the duty cycle d_p of the primary side upper switch S_{pv1}, as follows:

$$E_{p\_dc} = \frac{E_p}{d_p}. \tag{1}$$

On the secondary side of phase-V, when the DC link voltage is constant, it can be considered as a buck operation of the bidirectional chopper. The voltage across the capacitor C_{s_m}, denoted as E_{s_m} [V], can be expressed using the following equation, integrating the duty cycle d_s of the secondary side upper switch S_{sv1}:

$$E_{s\_m} = d_s E_s. \tag{2}$$

However, this paper aims to demonstrate the effectiveness of using the symmetric three-phase transformer; therefore, both primary and secondary duty cycles are fixed at $d_p = d_s = 0.5$. Under this condition, the circuit states of the active bridge are the four shown in Fig. 3. The operating modes in Fig. 3 correspond to the states (a)–(d) in Fig. 2. The voltage v_{p_v} [V] applied to the primary winding of the transformer, and the

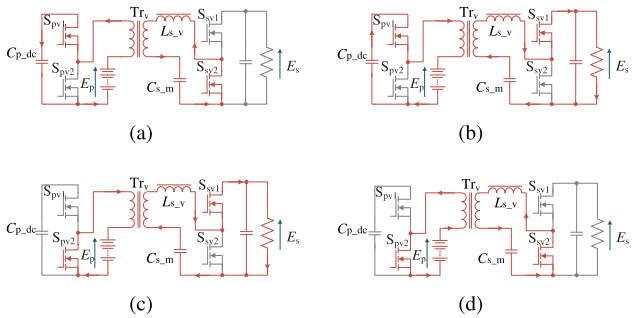

FIGURE 3. Operating diagrams of the proposed system in Mode V. **(a)** $0 \le \omega t \le \delta$. **(b)** $\delta \le \omega t \le \pi$. **(c)** $\pi \le \omega t \le \pi + \delta$. **(d)** $\pi + \delta \le \omega t \le 2\pi$.

voltage v_{s_v} [V] applied to the secondary phase-V winding and the series inductor L_{s_v}, and these voltages are represented by

$$v_p(\omega t) = \begin{cases} E_p & (0 \le \omega t \le \pi) \\ -E_p & (\pi \le \omega t \le 2\pi) \end{cases} \tag{3}$$

$$v_s(\omega t) = \begin{cases} \dfrac{E_s}{2} & (\pi \le \omega t \le \pi + \delta) \\ -\dfrac{E_s}{2} & (\omega t \le \pi,\ \pi + \delta \le \omega t) \end{cases} \tag{4}$$

where δ [rad] is the phase-shift angle and ω [rad/s] is switching angular frequency.

From the above (3) and (4), the current $i_{s\_v}(\omega t)$ [A] flowing through the series inductor L_{s_v} can be expressed as

$$i_{s\_v}(\omega t) = \frac{1}{L_{s\_v}} \int_0^{2\pi} \{N_v v_p(\omega t) - v_s(\omega t)\} d\omega t$$

$$= \begin{cases} \dfrac{2N_v E_p + E_s}{2\omega L_{s\_v}} \omega t + i_{s\_v}(0) & (0 \le \omega t \le \delta) \\ \dfrac{2N_v E_p - E_s}{2\omega L_{s\_v}} (\omega t - \delta) + i_{s\_v}(\delta) & (\delta \le \omega t \le \pi) \\ -\dfrac{2N_v E_p + E_s}{2\omega L_{s\_v}} (\omega t - \pi) + i_{s\_v}(\pi) & (\pi \le \omega t \le \pi + \delta) \\ -\dfrac{2N_v E_p - E_s}{2\omega L_{s\_v}} (\omega t - \pi - \delta) + i_{s\_v}(\pi + \delta) & (\pi + \delta \le \omega t \le 2\pi) \end{cases} \tag{5}$$

where $i_{s\_v}(0)$, $i_{s\_v}(\delta)$, $i_{s\_v}(\pi)$, and $i_{s\_v}(\delta + \pi)$ [A] represent the initial values in each state. The value i_{s_v} can be determined from $i_{s\_v}(0) = -i_{s\_v}(\pi)$ as follows:

$$i_{s\_v}(0) = -i_{s\_v}(\pi) = -\frac{2\pi N_v E_p + (\pi - 2\delta) E_s}{4\omega L_{s\_v}}. \tag{6}$$

Similarly, $i_{s\_v}(\delta)$ can be determined from the relation $i_{s\_v}(\delta) = -i_{s\_v}(\delta + \pi)$ as

$$i_{s\_v}(\delta) = -i_{s\_v}(\delta + \pi) = \frac{2(\pi - 2\delta)\pi N_v E_p + \pi E_s}{4\omega L_{s\_v}}. \tag{7}$$

These values, $i_{s\_v}(0)$, $i_{s\_v}(\delta)$, $i_{s\_v}(\pi)$, and $i_{s\_v}(\delta + \pi)$, represent the instantaneous current values at switching and can be used to determine ZVS. During the dead-time period, just before the secondary side switch S_{sv1} turns on, the current i_{s_v} flows from the source to the drain of S_{sv1} if $i_{s\_v}(\delta) > 0$. Consequently, the charge stored in the parasitical output capacitance of S_{sv1} is discharged, the drain–source voltage becomes 0 V, and ZVS turn-on can be achieved.

On the other hand, the primary-winding current $i_{p\_v}(\omega t)$ [A] consists of the load current $i_{p\_v\_DAB}(\omega t)$ [A] originating from the DAB converter operation, the DC current $I_{p\_v\_dc}$ [A] originating from the boost-chopper operation, and the magnetizing current $i_{p\_v\_m}$ [A]. $I_{p\_v\_dc}$ can be derived from the input power P_{in} [W] and the primary side voltage E_p as follows:

$$I_{p\_v\_dc} = \frac{P_{in}}{E_p}. \tag{8}$$

The magnetizing current $i_{p\_v\_m}(\omega t)$ is the current flowing in magnetizing inductance L_{m_v} [H]. The applied voltage for L_{m_v} is equal to the voltage applied to the primary phase-V winding of the transformer, as described by (3). Thus, $i_{p\_v\_m}(\omega t)$ can be represented as

$$i_{p\_v\_m}(\omega t) = \frac{1}{L_{m\_v}} \int_0^{2\pi} v_{p\_v} d\omega t$$

$$= \begin{cases} \dfrac{E_p}{L_{m\_v}} \omega t + i_{p\_v\_m}(0) & (0 \le \omega t \le \pi) \\ -\dfrac{E_p}{L_{m\_v}} (\omega t - \pi) + i_{p\_v\_m}(\pi) & (\pi \le \omega t \le 2\pi) \end{cases} \tag{9}$$

where $i_{p\_v\_m}(0)$ and $i_{p\_v\_m}(\pi)$ [A] denote the initial values for each phase. Then, the relation $i_{p\_v\_m}(0) = -i_{p\_v\_m}(\pi)$ is valid. Consequently, $i_{p\_v\_m}(0)$ is determined by

$$i_{p\_v\_m}(0) = -\frac{E_p}{2L_{m\_v}} \pi. \tag{10}$$

Additionally, the load current $i_{p\_v\_DAB}(\omega t)$, resulting from the DAB converter operation, can be expressed as the turn ratios N_v multiple of the current $i_{s\_v}(\omega t)$ flowing through the secondary side series inductor L_{s_v}. This relationship is represented using the turn ratios N_v of phase-V transformer as

$$i_{p\_v\_DAB}(\omega t) = N_v i_{s\_v}(\omega t). \tag{11}$$

From the above, the primary winding current $i_{p\_v}(\omega t)$ is the superimposition of the DC power supply $I_{p\_v\_dc}$ [A], $i_{p\_v\_m}$ [A], and the load current $i_{p\_v\_DAB}(\omega t)$ [A] as follows:

$$i_{p\_v}(\omega t) = i_{p\_v\_DAB}(\omega t) + I_{p\_v\_dc} + i_{p\_v\_m}$$
$$= N_v i_{s\_v}(\omega t) + I_{p\_v\_dc} + i_{p\_v\_m}. \tag{12}$$

Due to the DC current on the primary side, the ZVS (Zero Voltage Switching) range differs between the upper switch S_{pv1} and the lower switch S_{pv2}. Specifically, S_{pv1} conducts

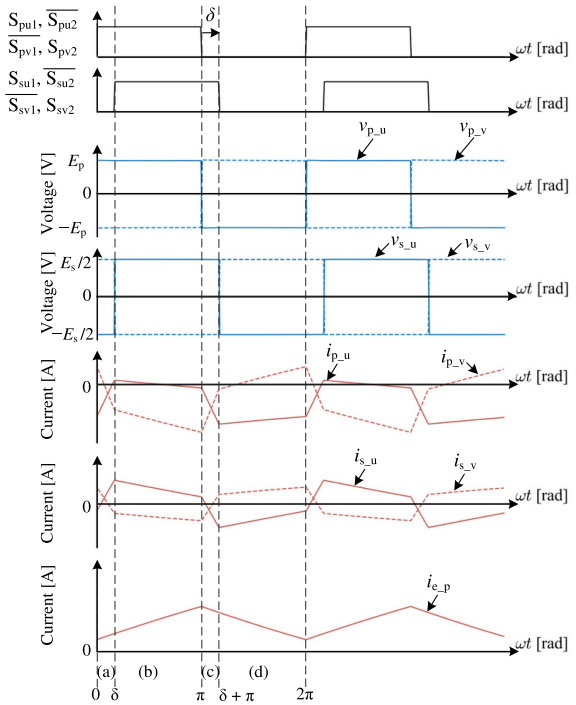

FIGURE 4. Operating waveforms of the proposed converter in Mode UV.

DC current from source to drain, while S_{pv2} conducts in the opposite direction from drain to source. In other words, the ZVS condition for S_{pv1} is $i(0) < 0$, thereby enabling ZVS operation over a very wide range. Conversely, for S_{pv2}, where the ZVS condition is $i_{p\_v}(\pi) > 0$, the ZVS range is more restricted compared to that of S_{pv1}.

Moreover, the output power, denoted as P_{out} [W], can be calculated by integrating the product of $v_{s\_v}(\omega t)$ and $i_{s\_v}(\omega t)$ over a switching period of 2π, as follows:

$$P_{out} = \frac{1}{2\pi}\int_0^{2\pi} v_{s\_v}(\omega t)\, i_{s\_v}(\omega t)\, d\omega t = \frac{N_v E_p E_s}{2\omega L_{s\_v}}\delta\left(1-\frac{\delta}{\pi}\right). \quad (13)$$

2) MODE UV

Fig. 4 shows the waveforms during Mode UV. In this mode, phase-U and phase-V are in an inverse relationship, while the legs in phase-W are halted by off-signals. By energizing the U and V phases simultaneously, the output power increases. As a result, the high-efficiency operating point shifts to the mid-load region. Consequently, the output power P_{out} can be described as the collective sum of the outputs of the two phases.

$$P_{out} = \frac{E_p E_s}{2\omega}\left(\frac{N_u}{L_{s\_u}} + \frac{N_{s\_v}}{L_{s\_v}}\right)\delta\left(1-\frac{\delta}{\pi}\right) \quad (14)$$

In this paper, the phase-shift angle δ between the primary and secondary sides in each phase is set to be equal and is denoted by δ [rad].

The AC currents for each component can be determined similarly to phase-V. On the other hand, the DC currents for the primary winding $I_{p\_u\_dc}$ and $I_{p\_v\_dc}$ [A] are ideally divided equally for the input power P_{in} as expressed by

$$I_{p\_u\_dc} = I_{p\_v\_dc} = \frac{P_{in}}{2E_p}. \quad (15)$$

By operating phase-U and phase-V opposite phases to each other, reducing the ripple of the input current i_{e_p} [A] from the power source is possible.

3) MODE UVW

In Mode UVW, each phase maintains a constant phase-shift angle of $2\pi/3$ rad. This approach effectively reduces the ripple in the input current i_{e_p} [A] from the source. In this operating mode, all three phases are operated in parallel, yielding a higher output power than when operated with single or dual-phase energization. Consequently, this scenario shifts the high-efficiency operation point toward the heavy-load range. The output power P_{out} can be represented as the sum of the three phases.

$$P_{out} = \frac{E_p E_s}{2\omega}\left(\frac{N_u}{L_{s\_u}} + \frac{N_v}{L_{s\_v}} + \frac{N_w}{L_{s\_w}}\right)\delta\left(1-\frac{\delta}{\pi}\right) \quad (16)$$

In this study, the phase-shift angle δ between the primary and secondary side bridges of each phase is made uniform, similar to Mode UV.

Additionally, the DC currents in the primary windings, which are represented as $I_{p\_u\_dc}$, $I_{p\_v\_dc}$, and $I_{p\_w\_dc}$ [A], are distributed evenly across the phases relative to the input power P_{in}. This distribution can be expressed by

$$I_{p\_u\_dc} = I_{p\_v\_dc} = I_{p\_w\_dc} = \frac{P_{in}}{3E_p}. \quad (17)$$

C. DESIGN GUIDELINE FOR TRANSFORMER AND SERIES INDUCTORS

It is assumed that the primary side DC voltage is $E_p = 30$–60 V, and the secondary side DC voltage is $E_s = 150$ V; thus, the range of the voltage ratio is from 2.5 to 5. When the duty cycles are set to a constant of 0.5, the DC-bus voltage relates as $E_{pdc} = 2E_p$. This implies that the ideal turn ratios of the transformer is approximately half of this voltage ratio. Thus, in this prototype, the turn ratios for the asymmetric three-phase transformer are set to $N_u = 1.25$, $N_v = 1.75$, and $N_w = 2.25$, respectively.

The asymmetric three-phase transformer used in the prototype is composed of three single-phase transformers connected. Fig. 6 shows the appearance of a single-phase transformer in the prototype. As mentioned earlier, in the proposed converter, the DC current I_{p_dc} [A] flows through the primary winding of the transformer. I_{p_dc} differs from the load current, and the flux due to I_{p_dc} does not cancel out with the flux generated on the secondary side. Therefore, in the

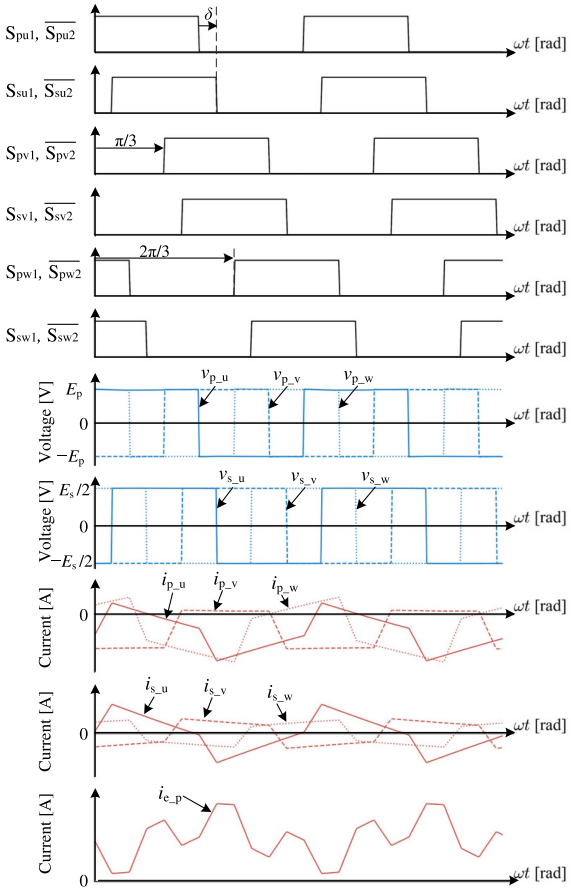

FIGURE 5. Operating waveforms of the proposed converter in Mode UVW.

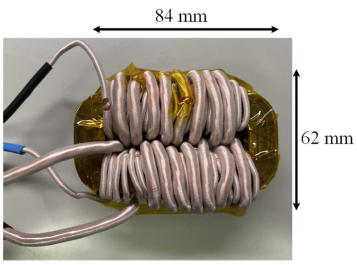

FIGURE 6. Appearance of a single-phase of the asymmetric three-phase transformer in the prototype of the proposed converter.

prototype, in addition to using core material with a high saturation flux density to prevent the transformer from reaching magnetic saturation, a total air gap of 2 mm is provided.

Furthermore, during two-phase and three-phase energization, to equalize the transmitted power of each phase, the turn ratios $N_{\rm u}$, $N_{\rm v}$, and $N_{\rm w}$ for the U, V, W phase transformers, as well as the series inductors $L_{\rm s\_u}$, $L_{\rm s\_v}$, and $L_{\rm s\_w}$, are designed to satisfy as follows:

$$\frac{N_{\rm u}}{L_{\rm s\_u}} = \frac{N_{\rm v}}{L_{\rm s\_v}} = \frac{N_{\rm w}}{L_{\rm s\_w}}. \tag{18}$$

TABLE 2. Circuit Parameters of the Proposed System

Input voltage $E_{\rm p}$	30 – 60 V
Output voltage $E_{\rm s}$	150 V
Switching frequency f	50 kHz
Duty cycles of the upper arms d	0.5
Rated output power $P_{\rm out}$	1.0 kW
Power devices	*Wolfspeed* CCS050M12CM2
On state resistance $r_{\rm on}$	25 mΩ
Turn-on switcihing energy $E_{\rm on}$ ($v_{\rm ds\_base}$ = 600 V, $i_{\rm d\_base}$ = 50 A)	1.1 mJ
Turn-off switcihing energy $E_{\rm off}$ ($v_{\rm ds\_base}$ = 600 V, $i_{\rm d\_base} = 50A$)	0.6 mJ
Transformers' cores	*Proterial* AMCC0040
Additional indactor cores	*TDK* PC47PQ32/30Z-12
primary side DC bus capacitor $C_{\rm p\_dc}$	50 μF, 0.55 mΩ
secondary side clamp capacitor $C_{\rm s\_m}$	140 μF, 0.85 mΩ

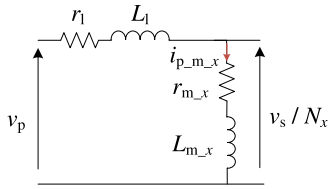

FIGURE 7. Equivalent model of a single phase-*X* of the three-phase transformer.

III. EFFICIENCY ANALYSIS OF PROPOSED CONVERTER

In this paper, a 1 kW prototype of the proposed converter is developed to validate its effectiveness. This chapter models and analyzes the prototype and then clarifies the characteristics and efficient operating modes.

A. MODELING OF PROTOTYPE

In this section, the prototype is modeled for the efficiency analysis. The circuit parameters specific to the prototype are detailed in Table 2. Meanwhile, parameters regarding the transformer are shown in Table 3. The parameters in Table 3 are measured using the LCR meter (*HIOKI* IM3536). Constants labeled "open" represent measured values at 50 kHz when the primary winding is connected to the LCR meter and the secondary winding is left open. On the other hand, those labeled "short" represent measured values at 50 kHz when the secondary side is shorted.

1) MODELING OF TRANSFORMERS

Fig. 7 shows an equivalent model of a phase-*X* of the three-phase transformer. It is important to note that in Fig. 7, the parameters of the secondary side of the transformer are referred to the primary side. The magnetizing inductance of

TABLE 3. Measured Circuit Parameters of the Transformers in the Proposed Converter At 50 Khz for the Modeling

	$\mathrm{Tr_u}$	$\mathrm{Tr_v}$	$\mathrm{Tr_w}$
Number of turns in the primary side $n_{\mathrm{p\_u}}$, $n_{\mathrm{p\_v}}$, $n_{\mathrm{p\_w}}$	16	16	16
Number of turns in the secondary side $n_{\mathrm{s\_u}}$, $n_{\mathrm{s\_v}}$, $n_{\mathrm{s\_w}}$	20	28	36
Inductances when the secondary winding is open $L_{\mathrm{open\_u}}$, $L_{\mathrm{open\_v}}$, $L_{\mathrm{open\_w}}$ [μH]	69.8	65.7	66.5
Inductances when the secondary winding is shorted $L_{\mathrm{short\_u}}$, $L_{\mathrm{short\_v}}$, $L_{\mathrm{short\_w}}$ [μH]	2.61	2.12	2.78
ESRs when the secondary winding is open $r_{\mathrm{open\_u}}$, $r_{\mathrm{open\_v}}$, $r_{\mathrm{open\_w}}$ [Ω]	0.59	0.56	0.57
ESRs when the secondary winding is shorted $r_{\mathrm{short\_u}}$, $r_{\mathrm{short\_v}}$, $r_{\mathrm{short\_w}}$ [mΩ]	54.2	36.4	35.3
ESRs of the transformers (DC) $r_{\mathrm{dc\_u}}$, $r_{\mathrm{dc\_v}}$, $r_{\mathrm{dc\_w}}$ [mΩ]	5.99	5.57	6.14
Inductances of the additional inductors $L_{\mathrm{add\_u}}$, $L_{\mathrm{add\_v}}$, $r_{\mathrm{add\_w}}$ [mΩ]	13.2	16.6	6.14
ESRs of the additional inductors $r_{\mathrm{L\_c\_u}}$, $r_{\mathrm{L\_c\_v}}$, $r_{\mathrm{L\_c\_w}}$ [mΩ]	73.9	41.3	53.5
Coupling coefficients k_{u}, k_{v}, k_{w}	0.98	0.98	0.98
Effective series inductances $L_{\mathrm{s\_u}}$, $L_{\mathrm{s\_v}}$, $L_{\mathrm{s\_w}}$ [μH]	17.3	23.0	30.0

the transformer in the proposed converter is low, leading to a substantial magnetizing current flow. Therefore, an equivalent series model is adopted for the magnetizing resistance r_{m_x} [Ω] in this analysis. However, the magnetizing inductance L_{m_x} [H] and magnetizing resistance r_{m_x} for phase-X cannot be directly measured with the LCR meter. Instead, they are modeled using the inductance L_{open_x} and resistance r_{open_x} from when the secondary winding is opened, along with the coupling coefficient k. However, since the LCR meter represents the total loss of the test component as an equivalent single resistance, the core loss resistance (magnetizing resistance), while simplistic, includes both hysteresis and eddy current losses.

$$L_{\mathrm{m}\_x} = kL_{\mathrm{open}\_x} \tag{19}$$

$$r_{\mathrm{m}\_x} = kr_{\mathrm{open}\_x} \tag{20}$$

The leakage inductance L_{l_x} [H] and ESR (; equivalent series resistance) r_{l_x} [Ω] in phase-X of the transformer are based on L_{short_x} [H] and r_{short_x} [Ω] obtained when the secondary winding is shorted, hence the following relationship exists.

$$L_{\mathrm{l}\_x} = L_{\mathrm{short}\_x} \tag{21}$$

$$r_{\mathrm{l}\_x} = r_{\mathrm{short}\_x} \tag{22}$$

In the proposed converter, an inductor L_{add_x} [H] is additionally connected to regulate the output power. Therefore, the inductance L_{s_x} [H] that effectively contributes to the output power can be expressed as follows:

$$L_{\mathrm{s}\_x} = N_x^2 L_{\mathrm{l}\_x} + L_{\mathrm{add}\_x}. \tag{23}$$

Note that N_x represents the turn ratios of the transformer for phase X.

2) POWER-LOSS MODELS

The power loss in the proposed converter comprises conduction and switching losses in the power devices, as well as core and winding losses in the transformers and inductors. In this section, the details of the loss models employed in the analysis in the next chapter are explained. For this analysis, the resistances on the PCBs and the ESRs of the capacitors are considered sufficiently small and ignored.

The conduction loss, denoted as P_{con_x} [W], in a power device S_x can be represented by

$$P_{\mathrm{con}\_x} = r_{\mathrm{on}} I_{\mathrm{con}\_x}^2, \tag{24}$$

where r_{on} is the on-resistance of the power devices and I_{con_x} is the RMS value of the drain current.

On the other hand, the switching loss of the power device S_x represented as P_{sw_x} [W], can be modeled as follows:

$$P_{\mathrm{sw}\_x} = \frac{v_{\mathrm{ds\_sw}} i_{\mathrm{d\_sw}}}{v_{\mathrm{ds\_base}} i_{\mathrm{d\_base}}} f E_{\mathrm{sw}}, \tag{25}$$

where E_{sw} [J] is the switching loss based on the data sheet and f [Hz] is the switching frequency.

$v_{\mathrm{ds\_base}}$ [V] and $i_{\mathrm{d\_base}}$ [A] are the specific drain–source voltage and drain current based on the double pulse test as specified in the datasheet, respectively. Meanwhile, $v_{\mathrm{ds\_sw}}$ [V] and $i_{\mathrm{d\_sw}}$ [A] represent the drain–source voltage and drain current, respectively, at the instance of switching at the analysis point. As shown by (25), this paper simplistically models switching loss using a ratio compared to the datasheet values. Furthermore, (25) can represent both turn-on and turn-off losses.

The core loss of phase-X transformer, denoted as $P_{\mathrm{tr\_core}\_x}$ [W], is modeled based on

$$P_{\mathrm{tr\_core}\_x} = r_{\mathrm{m}\_x} I_{\mathrm{p\_m}\_x}^2, \tag{26}$$

where $I_{\mathrm{p\_m}\_x}$ [A] is the RMS value of the magnetizing current.

The winding loss in phase-X transformer, represented as $P_{\mathrm{tr\_wire}\_x}$ [W], is modeled based on the losses caused by the AC and DC currents. To calculate $P_{\mathrm{tr\_wire}\_x}$, the RMS values of the load current $I_{\mathrm{p}\_x\_\mathrm{dab}}$ [A], magnetizing current $I_{\mathrm{p}\_x\_\mathrm{m}}$ [A], and DC current $I_{\mathrm{p}\_x\_\mathrm{dc}}$ [A] are used. In addition, the winding resistance r_{s_x} [Ω] of the transformer at the switching frequency of 50 kHz and the primary winding resistance r_{dc_x} [Ω] at DC current are used as follows:

$$P_{\mathrm{tr\_wire}\_x} = r_{\mathrm{s}\_x}\left(I_{\mathrm{p}\_x\_\mathrm{dab}}^2 + I_{\mathrm{p}\_x\_\mathrm{m}}^2\right) + r_{\mathrm{dc}\_x} I_{\mathrm{p}\_x\_\mathrm{dc}}^2. \tag{27}$$

In phase-X, the winding loss of the inductor, denoted as $P_{\mathrm{L\_wire}\_x}$ [W], is calculated using its ESR at the switching

frequency 50 kHz, represented as r_{L_wire} [Ω]. This power loss can be calculated using the current I_{s_x} [A] flowing through the series inductor L_{s_x} as follows:

$$P_{L\_wire\_x} = r_{L\_c\_x} I_{s\_x}^2. \tag{28}$$

Here, P_{total_loss} [W] is the total loss in the proposed converter and is represented by the following equation.

$$P_{total\_loss} = \sum_x P_{con\_x} + \sum_x P_{sw\_x} + \sum_x P_{tr\_core\_x} + \sum_x P_{tr\_wire\_x} + \sum_x P_{L\_wire\_x} \tag{29}$$

In the subsequent chapter, the variables are defined as $P_{sw} = \sum_x P_{sw\_x}$, $P_{tr\_core} = \sum_x P_{tr\_core\_x}$, $P_{tr\_wire} = \sum_x P_{tr\_wire\_x}$, $P_{L\_wire} = \sum_x P_{L\_wire\_x}$ [W] for simplicity.

The efficiency of the proposed converter η [%] is defined by

$$\eta = \frac{100 P_{out}}{P_{out} + P_{total\_loss}}. \tag{30}$$

B. OVERVIEW OF EFFICIENCY CHARACTERISTICS

This section presents the efficiency characteristics and the power loss breakdown of the proposed converter using the power loss model presented in this chapter. It is assumed that the primary side voltage E_p varies from 30 to 60 V, the secondary side voltage E_s is fixed at 150 V, and the output power ranges from 0 to 1 kW (1 p.u.).

Fig. 8 shows the ZVS operating range and efficiency characteristics in each mode. The ZVS operating boundary in Fig. 8 is marked with a dotted line. For example, in Mode V in Fig. 8(b), the primary side switches S_{pv1} and S_{pv2} can achieve ZVS operation when the primary voltage E_p is higher than the boundary. Conversely, the secondary side switches S_{sv1} and S_{sv2} achieve ZVS operation when E_p is lower than the boundary.

The secondary side active bridge achieves ZVS operation similar to general DAB converters. In the primary side active bridge, due to the DC current $I_{p\_v\_dc}$ as defined in (8), the ZVS operation ranges are different between the upper switch S_{pv1} and the lower switch S_{pv2}.

S_{pv1} can achieve ZVS across a broad range since the DC current $I_{p\_v\_dc}$ flows from the source to the drain. On the other hand, S_{pv2} can achieve ZVS across an extensive voltage ratio under light loads due to the triangular waveform of magnetizing current $i_{p\_v\_m}$. However, the DC current $I_{p\_v\_dc}$ from the drain to the source under heavier loads becomes more prevalent, and the ZVS operating range shrinks.

It is suggested that expanding the ZVS operating range of switches S_{pv1} and S_{pv2} is possible by reducing the magnetizing inductance L_{m_v} and increasing $i_{p\_v\_m}$. However, there is a trade-off to consider related to conduction losses.

The tendencies of the ZVS operating ranges in Mode U and Mode W can also be explained in the same way as in Mode V. However, in Mode U, S_{su1} and S_{su2} switch with ZVS even at $E_p = 60$ V because the turn ratios of Tr_u is small. Therefore, in Fig. 8(a), S_{su1} and S_{su2} switch with ZVS in all operating ranges. Furthermore, Fig. 8(d), (e), and (f) show that the ZVS operating range becomes the combined one of each ZVS operating range due to the phase decoupling when multiple phases are energized.

In Fig. 9, the efficiencies of all operating modes shown in Fig. 8 are compared, and the results of selecting the operating mode with the maximum efficiency and its efficiency characteristics are presented. Fig. 9 shows that higher efficiency is achieved in the operating modes where the transformers with a turn ratios close to $E_s/(2E_p)$ are selected according to the voltage ratio. In operating regions with a high primary voltage E_p, E_s/E_p becomes smaller, leading to the selection of operating Modes U and UV, which energize the transformer Tr_u with a lower turn ratios. Conversely, as E_p decreases, E_s/E_p increases, operating Modes W and VW, which energize the transformer Tr_w, are selected.

Concerning the load, the following trends are observed. At light loads, the current flowing through the converter is small, and the switching and core losses dominate. Therefore, energizing only one phase with fewer switches and transformers is more efficient. On the other hand, since the conduction loss becomes dominant under heavy load, the efficiency can be improved by energizing multi-phases and shunting current.

Furthermore, the DC current becomes large in the operating range where E_p is low. Thus, energizing three phases and diverting the DC current is more efficient.

C. POWER LOSS BREAKDOWN

In this section, the power loss breakdown is shown. Here, the power losses, using the model employed in the previous chapter, are categorized: conduction losses P_{con} and switching losses P_{sw} from the power devices, core losses P_{tr_core} and winding losses P_{tr_wire} from the transformers, and the loss P_{L_wire} from the additional inductors.

1) MODE V

Fig. 10 shows the breakdowns of power losses in Mode V at $P_{out} = 0.1$, 0.3, and 0.5 p.u. From Fig. 10(a), at lighter loads ($P_{out} = 0.1$ p.u.), P_{sw} is dominated, and the total losses are minimized when $E_p = E_s/(2N_v) = 43$ V. On the other hand, from Fig. 10(b) and (c), as the heavier load at $P_{out} = 0.3$ and 0.5 p.u., the losses of P_{con} and P_{tr_wire}, which are proportional to the square of the current, become more dominant. This is because, as shown in (8), the DC current $I_{p\_v\_dc}$ relative to the input power P_{in} increases when E_p is low, increasing conduction losses on the primary side. This implies that as the load increases, the minimum loss point moves to the higher voltage side of E_p.

The power loss characteristics of Modes U and W can be similarly described.

2) MODE UV

Fig. 11 shows the power-loss breakdown in Mode UV at $P_{out} = 0.1$, 0.5, and 1 p.u. As observed in Fig. 11(a), under

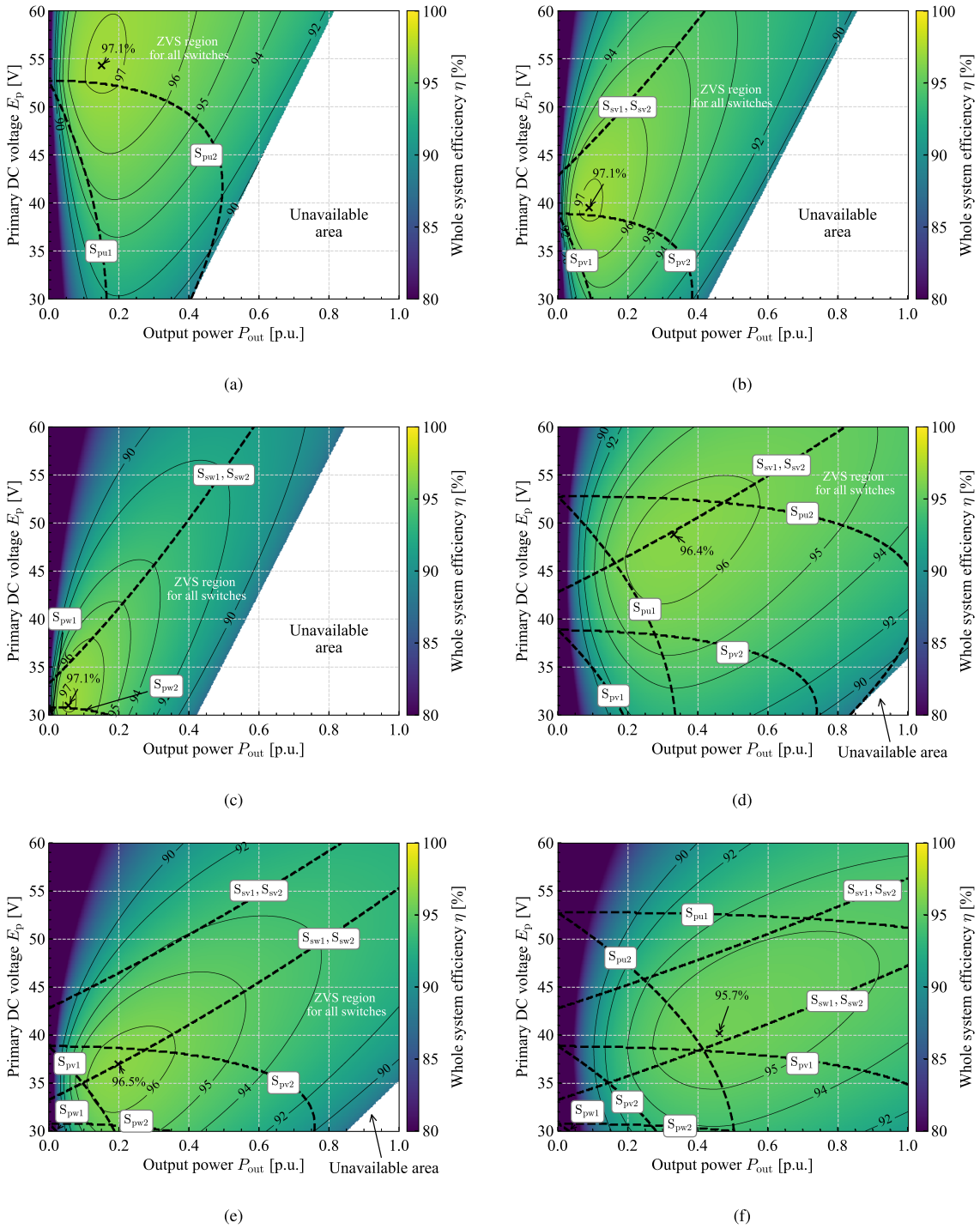

FIGURE 8. ZVS and efficiency characteristics of the proposed converter. (a) Mode U. (b) Mode V. (c) Mode W. (d) Mode UV. (e) Mode VW. (f) Mode UVW.

light load conditions ($P_{out} = 0.1$ p.u.), the switching losses P_{sw} increases compared to Mode V, where only one phase is energized. This is due to the higher number of power devices being driven.

Conversely, under medium load conditions ($P_{out} = 0.5$ p.u.), when compared to Mode V as shown in Fig. 10(c), the current is distributed among the phases. This leads to a reduction in both P_{con} and P_{tr_wire}, resulting in improved efficiency. Additionally, P_{con} increases when E_p is lower, similar to Mode V. However, in the operating region close to 60 V for E_p, the secondary side of phase-V exits the ZVS operating range, increasing in P_{sw}. Furthermore, as E_p increases, P_{tr_core} also increases because the magnetizing current on the primary side increases. From these

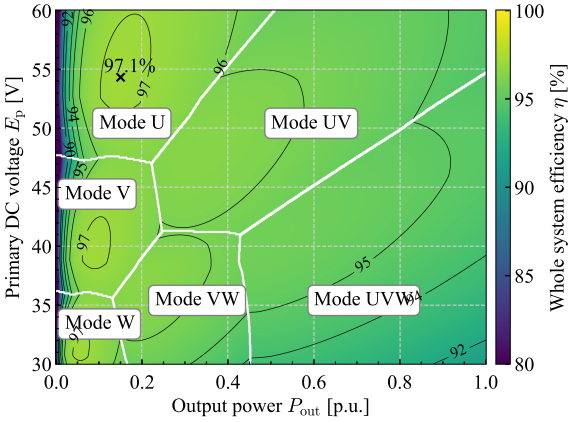

FIGURE 9. Selected efficient operating mode for each operating point.

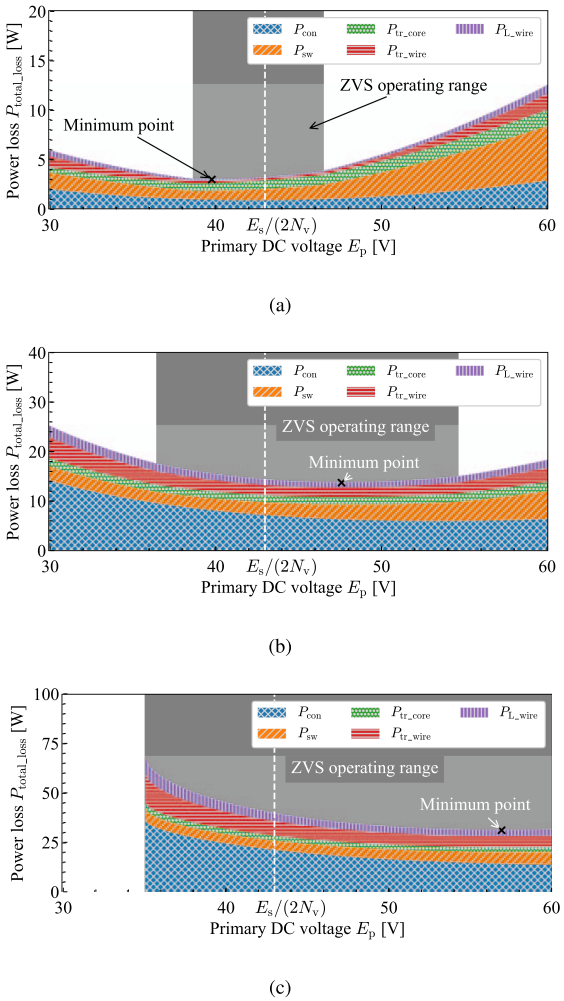

FIGURE 10. Power loss breakdown of the proposed converter in Mode V. (a) $P_{out} = 0.1$ p.u. (b) $P_{out} = 0.3$ p.u. (c) $P_{out} = 0.5$ p.u..

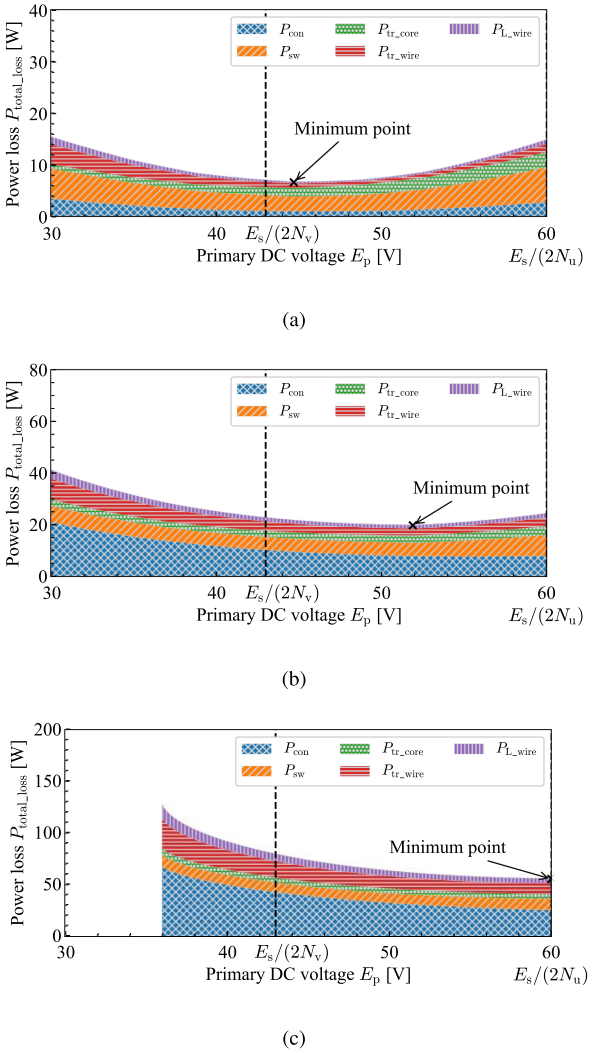

FIGURE 11. Power loss breakdown of the proposed converter in Mode UV. (a) $P_{out} = 0.1$ p.u. (b) $P_{out} = 0.5$ p.u. (c) $P_{out} = 1$ p.u..

characteristics, under medium loads, the converter operates efficiently in the range $E_s/(2N_v) < E_p < E_s/(2N_u)$ [V], or more specifically, 43 V $< E_p <$ 60 V.

At full load ($P_{out} = 1$ p.u.), as shown in Fig. 11(c), the conduction losses P_{con} and the winding losses P_{tr_wire} become dominant. Moreover, in regions with a lower E_p, the DC current relative to the input power P_{in} becomes larger. Then, the conduction losses on the primary side increase. Therefore, the total loss P_{total_loss} decreases monotonically with an increase in E_p. As shown in Fig. 11(c), the total power loss reaches its minimum at $E_p = 60$ V. From the above, it can be said that Mode UV is effective under medium to heavy load conditions and within a high primary voltage range.

The power loss characteristics of Mode VW can be similarly described.

3) MODE UVW

Fig. 12 shows the power loss breakdown in Mode UVW at $P_{out} = 0.1$, 0.5, and 1 p.u. In all operating ranges shown in Fig. 12, since all three phases are active, the proportion of switching losses P_{sw} and core losses P_{tr_core} increases compared to other modes. On the other hand, Mode UVW, which distributes the current among all three phases, becomes the

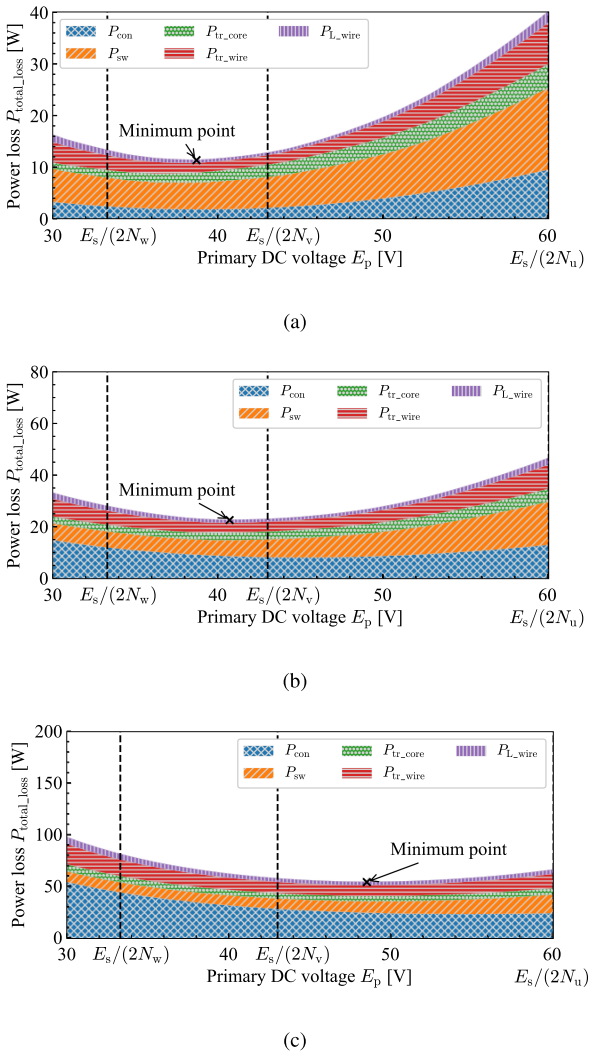

FIGURE 12. Power loss breakdown of the proposed converter in Mode UVW. (a) $P_{\text{out}} = 0.1$ p.u. (b) $P_{\text{out}} = 0.5$ p.u. (c) $P_{\text{out}} = 1$ p.u..

most efficient under medium to high loads where conduction losses dominate. Particularly in the operating range with a lower E_{p}, where the DC current I_{pdc} is large, the effect of the three-phase operation is pronounced.

However, in some ranges, the efficiency of Mode UVW is lower compared to Mode UV. This is because when E_{p} is high, the power devices on the secondary side of phase-W operate with hard switching, increasing in P_{sw}. Given these characteristics, Mode UVW is effective under heavy-load conditions with a lower primary side voltage E_{p}.

Based on the above analysis, the proposed converter can operate with high efficiency over a wide range by selecting energizing phases according to the load and voltage ratio using the asymmetric three-phase transformer.

IV. EXPERIMENT

In this chapter, the effectiveness of the proposed converter is demonstrated by observing operating waveforms and measuring efficiency using the 1 kW prototype shown in Fig. 13. The

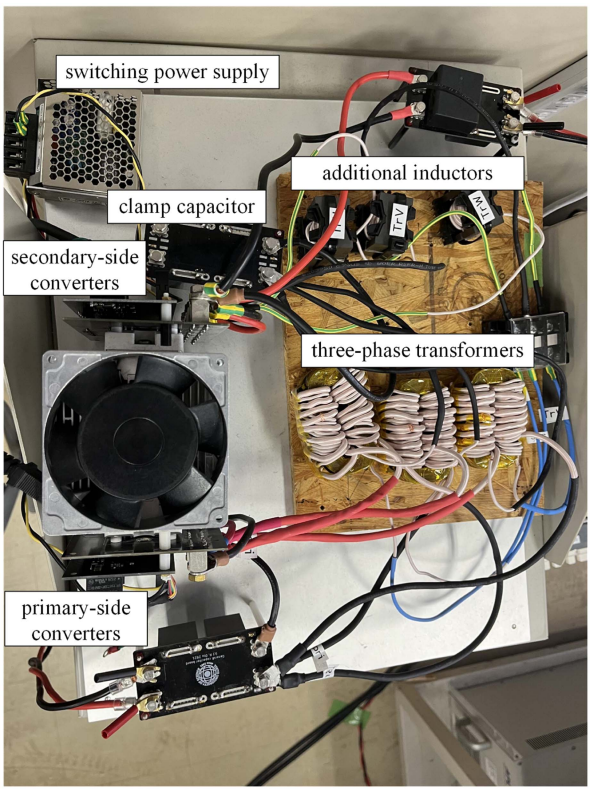

FIGURE 13. Appearance of the prototype of the proposed converter.

circuit parameters adopted for this prototype are detailed in Tables 2 and 3. These waveforms are measured with an oscilloscope (*Tektronix* MSO58), while the power and efficiency are measured using a power analyzer (*HIOKI* PW6001).

A. OPERATING WAVEFORMS

Fig. 14 shows the experimental waveforms in Mode V, Mode UV, and Mode UVW. In Fig. 14, the points where the phase-shift angle between the primary-side and secondary-side voltages is represented as $\delta = \pi/6$ rad. From Fig. 14, the experimental waveforms in Mode V, Mode UV, and Mode UVW show similar trends to the theoretical waveforms in Figs. 2, 4, and 5. Furthermore, from Fig. 14(b) and (c), it can be observed that the waveforms during multi-phase energization are composed of the waveforms during single-phase energization. From this, it can be confirmed that each phase in the converter is decoupled.

Additionally, as shown in Fig. 14(c), the DC component of the primary-side current in each phase is observed to be 7.60 A for phase-U, 7.24 A for phase-V, and 9.16 A for phase-W, respectively. While the prototype was not specifically designed for balanced current distribution, the DC components of the currents are somewhat evenly distributed.

B. EFFICIENCY CHARACTERISTICS

Fig. 15 shows the efficiency characteristics for each operating mode when E_{p} is 30, 40, 50, and 60 V. In the experiments, the

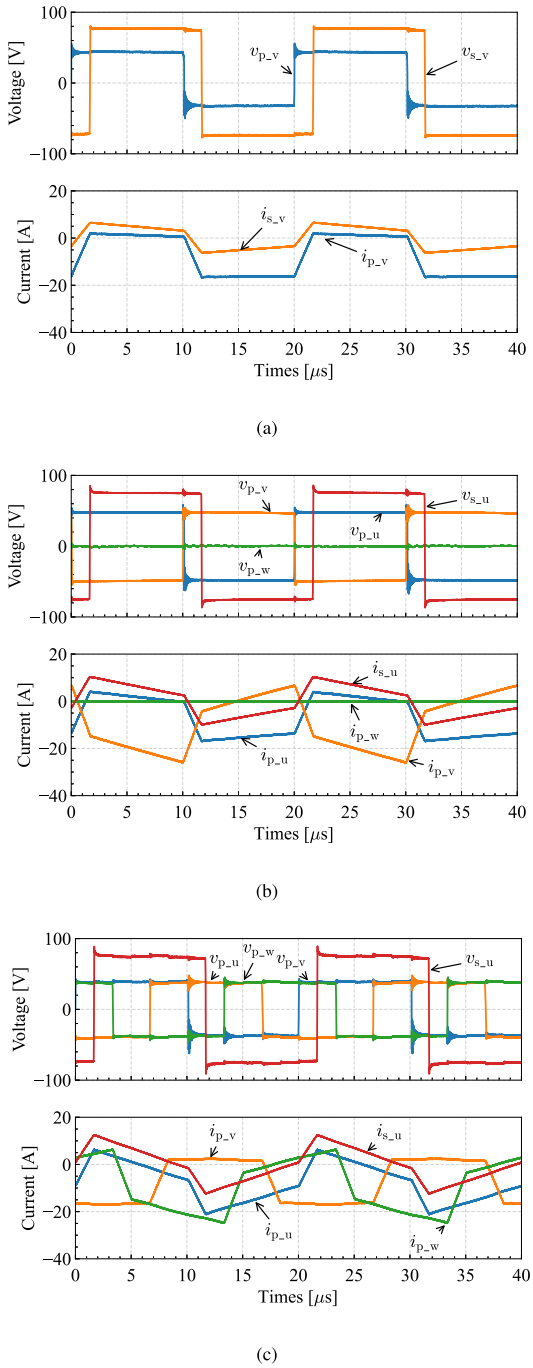

FIGURE 14. Experimental waveforms of the voltages and currents in the proposed converter for each operating mode. (a) Mode V(P_{out} = 0.28 p.u., E_p = 40 V). (b) Mode UV(P_{out} = 0.75 p.u., E_p = 50 V). (c) Mode UVW(P_{out} = 0.89 p.u., E_p = 40 V).

characteristics are measured by varying the phase-shift angle δ from $\pi/36$ to $7\pi/18$ rad. As observed from Fig. 15, similar to the analysis results from the previous chapter, in the range of lower E_p (i.e., $E_p = 30, 40$ V), Mode V and Mode W operate with high efficiencies. Conversely, in the range of higher E_p, Mode U operates with high efficiency.

In addition, the following characteristics are shown for the load. At light loads, the highest efficiency is obtained when operated single-phase. On the other hand, dual-phase or three-phase operating is more efficient for heavy loads. The mode that reaches the maximum efficiency is consistent with that in the analytical results shown in Fig. 9, indicating the validity of the theoretical analysis.

However, for simplicity in this paper, temperature variations in power devices are not considered. The power losses in magnetic components are calculated using the ESRs measured at the operating frequency by an LCR meter. Therefore, the theoretically derived power losses tend to be lower than the measured values. In practice, besides these losses, there may be an increase in losses due to temperature variations in the power devices and the magnetic components, as well as core losses due to harmonic components of currents. Accurate methods for calculating these losses are described in references [27], [28]. However, this paper emphasizes confirming the effectiveness of the proposed converter and, therefore, does not delve into complex analyses. Nonetheless, even when using the simplified model presented in Chapter 4, similar trends to the theoretical analysis are shown, indicating the validity of the theoretical analysis.

V. COMPARISON WITH THREE-PHASE DAB CONVERTER WITH SYMMETRIC TRANSFORMER

This chapter presents the efficiency characteristics of the DAB converter with an equal turn ratios across its three-phase transformer. In this paper, the converter with the symmetric three-phase transformer is called the conventional converter. Furthermore, by comparing these characteristics with those of the proposed converter, the effectiveness and characteristics of the proposed converter are clarified. In this comparison, the turn ratios in each phase of the conventional converter is set equal to that of phase-V. Furthermore, in the conventional converter, the operating modes considered are those where only one phase is energized or two phases are energized, as well as the proposed converter.

Fig. 16 shows the theoretical efficiency characteristics of the conventional converter, which is derived using the theoretical power-losses models. Fig. 17 illustrates the efficiency difference between the proposed and conventional converters, represented as $\eta - \eta_0$% points. As indicated by Fig. 16, the conventional converter operates with high efficiency in the range close to $E_p = E_s/(2N_v)$ [V] and under medium to heavy loads. However, outside this range, the efficiency of the conventional converter significantly drops, especially under lighter loads where the efficiency difference can exceed five % points.

Interestingly, within the high-efficiency operating range of the conventional converter ($E_p = E_s/(2N_v)$), the difference from the proposed converter peaks at a mere 1.25% points. It can be said that the efficiency drop caused by using an asymmetric transformer in the proposed converter is small.

In Fig. 18, the power losses of the two converters are compared. As shown in Fig. 18(a), the conventional converter,

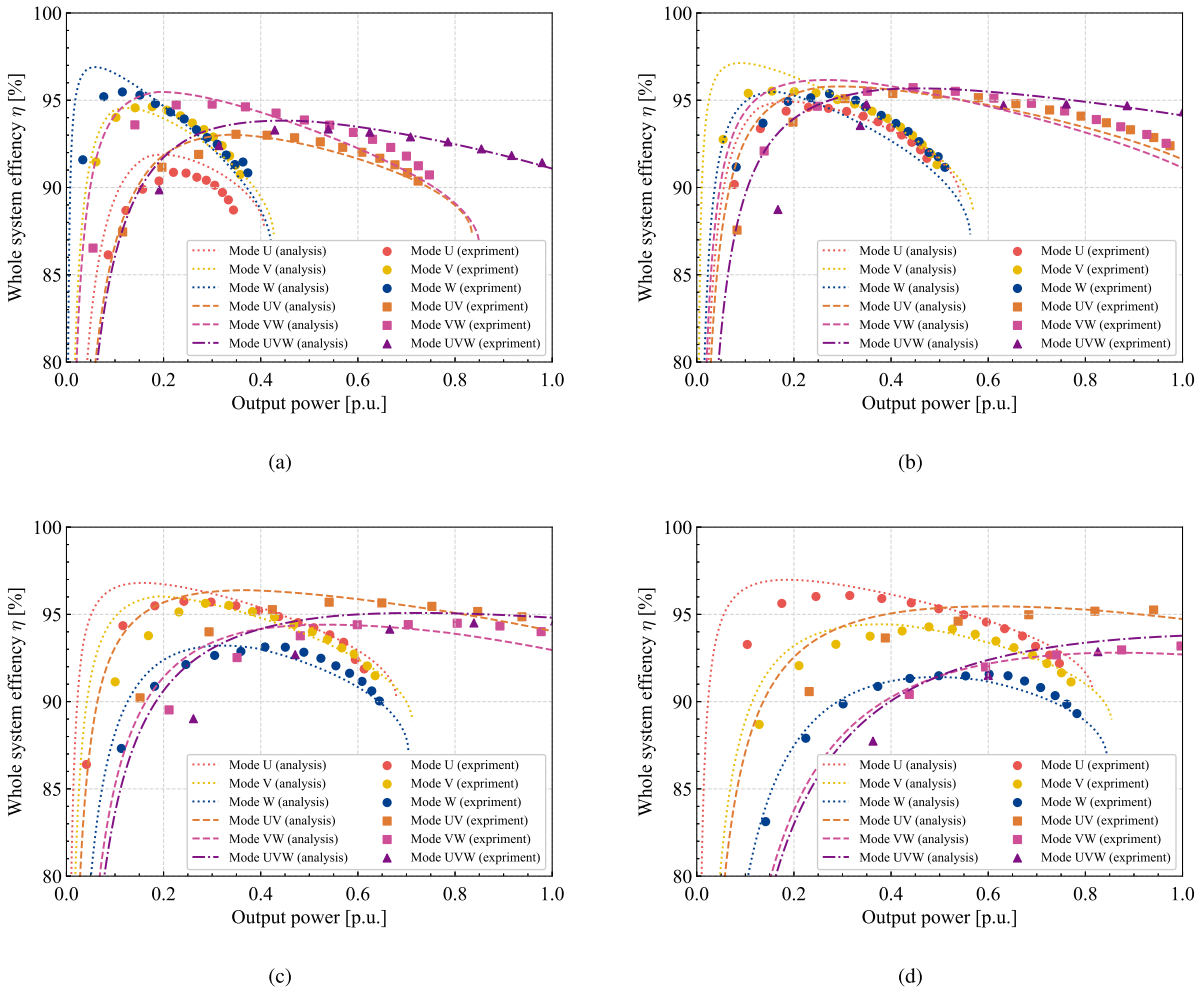

FIGURE 15. Whole-system efficiency in the analysis and experiment. (a) $E_p = 30$ V. (b) $E_p = 40$ V. (c) $E_p = 50$ V. (d) $E_p = 60$ V.

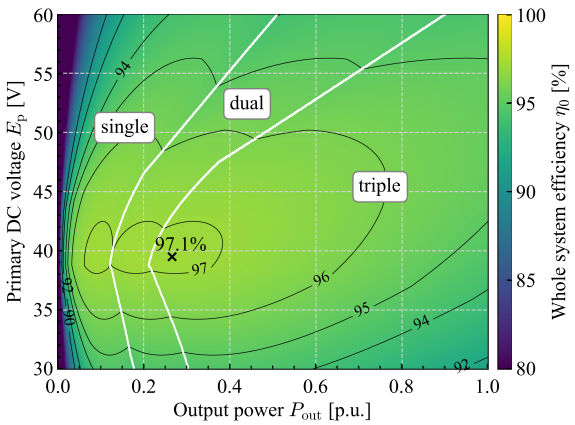

FIGURE 16. Theoretical efficiency characteristic of the conventional three-phase current-fed DAB converter with a symmetric transformer.

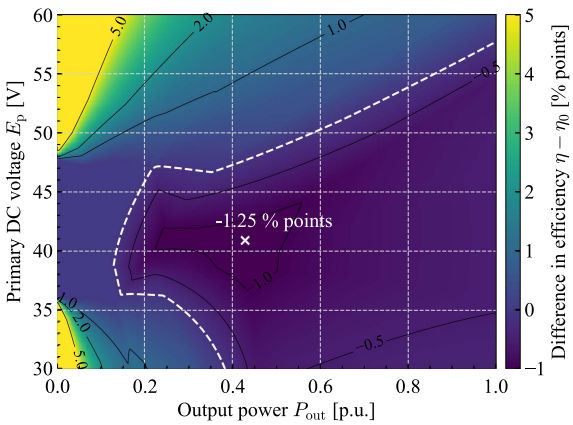

FIGURE 17. Efficiency difference between the proposed and conventional converters, represented as $\eta - \eta_0$.

when deviating from the ideal $E_p = E_s/(2N_v)$ [V] range, witnesses significant increases in both P_{con} and P_{sw}. This increase becomes more pronounced at E_p values beyond 50 V, caused by hard switching and an increase in reactive currents. On the other hand, the proposed converter suppresses the increase in P_{con} and P_{sw} by selecting the energizing phase according to E_p.

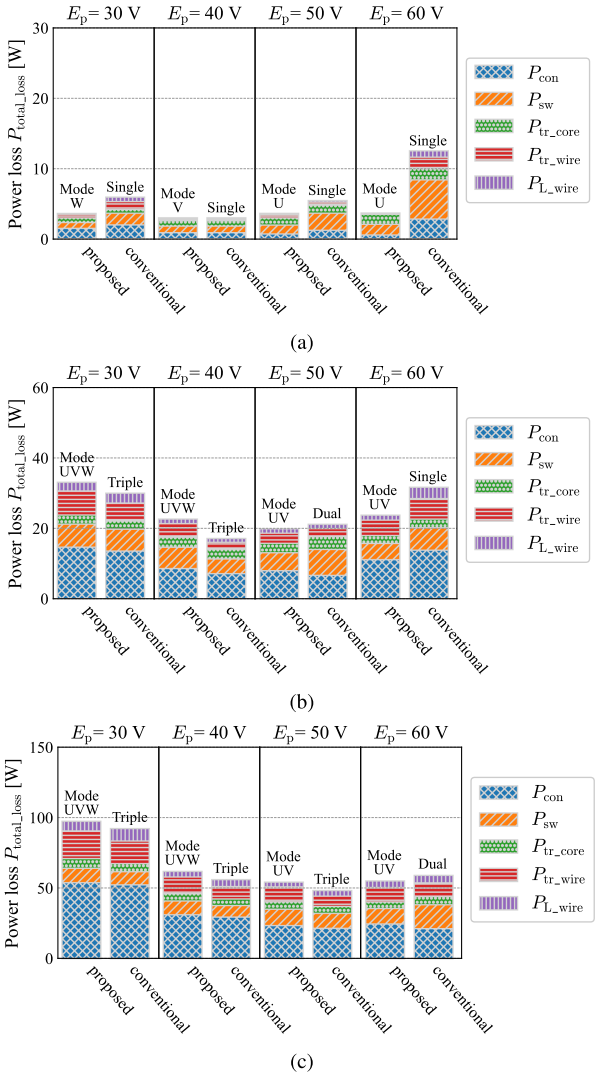

FIGURE 18. Power loss breakdown of the proposed/conventional converters. (a) $P_{out} = 0.1$ p.u. (b) $P_{out} = 0.5$ p.u. (c) $P_{out} = 1$ p.u..

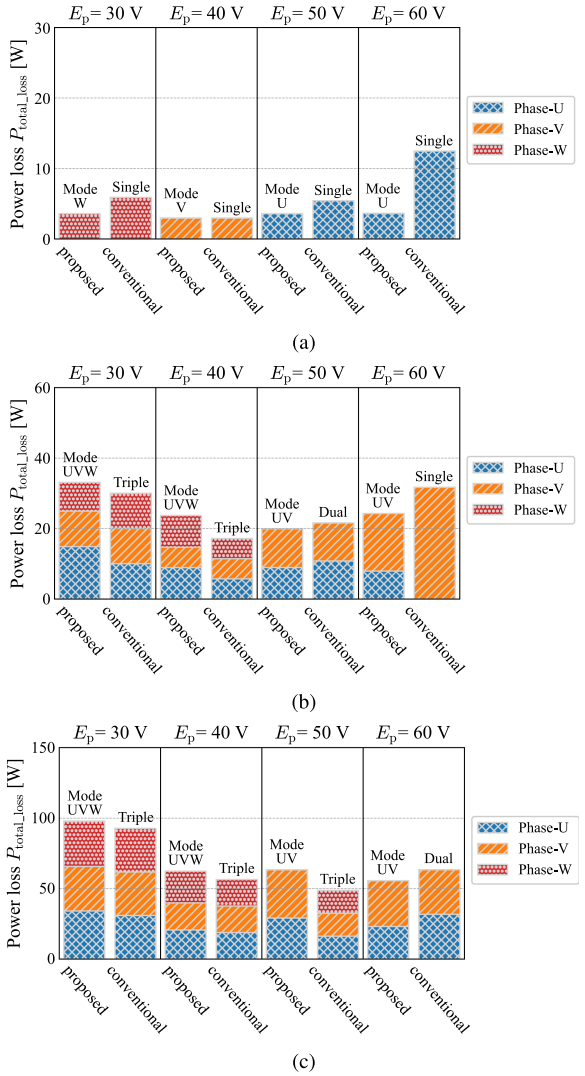

FIGURE 19. Power loss breakdown of the proposed/conventional converters. (a) $P_{out} = 0.1$ p.u. (b) $P_{out} = 0.5$ p.u. (c) $P_{out} = 1$ p.u.

In Fig. 18(b), at $E_p = 30$ and 40 V, the total loss is slightly smaller in the conventional converter. This is because, in the operating region where E_p is low, the conduction losses caused by currents become dominant. The conventional converter mitigates these power losses by energizing all three phases. The conventional converter evenly distributes these power losses across its three phases. However, even when all three phases are energized in the proposed converter, the total loss increases due to the increase in reactive current in phase-U and the hard switching. This phenomenon is prominent at $E_p = 30,\ 40$ V. On the other hand, for the proposed converter, at $E_p = 50$ and 60 V, the operating range is close to the $E_p = E_s/(2N_u)$ range in phase-U. Thus, reactive currents are reduced, thereby reducing conduction and switching losses.

In Fig. 18(c) for $E_p = 30$, 40, and 50 V, all three phases in both converters are energized. In the proposed converter, the phase with a deviated voltage ratio and turn ratios increases power losses, resulting in decreased efficiency. However, at $E_p = 60$ V, where only two phases are active in both converters, the proposed converter operates more efficiently than the conventional converter. This is because, similar to the case at $P_{out} = 0.5$ p.u., the reactive current flowing through phase-U is reduced, resulting in reduced conduction and switching losses.

Furthermore, Fig. 19 shows the breakdown of power losses for each phase of the proposed and conventional converters. Fig. 19 reveals that the power losses in each phase of the proposed converter exhibit an imbalance. This imbalance, particularly evident under medium to heavy loads within the medium voltage-ratio range, appears to negatively impact the efficiency of the proposed converter. However, for simplicity, the prototype employs a 6-in-1 power module, windings of uniform thickness, and magnetic cores of uniform size in each phase. For this, optimizing active/passive components for each phase enables the proposed converter to enhance efficiency without incurring significant costs. This approach

is anticipated to mitigate the efficiency gap between the proposed and conventional converters under medium to heavy loads within the medium voltage-ratio range.

From the above, it can be said that the proposed converter can maintain high efficiency over a wide operating range compared to the conventional converter with the symmetric three-phase transformer. Moreover, the efficiency drop at the operating range defined by $E_p = E_s/(2N_v)$ is capped at 1.25% points. In other words, it is clarified that efficiency drops are minimal even when using an asymmetrical three-phase transformer. Therefore, the effectiveness of selecting operating modes according to the voltage ratio and load has been demonstrated.

VI. CONCLUSION

This paper proposed a current-fed DAB converter with an asymmetric three-phase transformer. The proposed converter can expand the efficient operating range and improve the facility utilization of the transformer. The proposed converter has six operating modes and can select/combine the operating mode depending on the input-output voltage ratio and load.

In Chapter 3, the guidelines for selecting the efficient operating mode and the efficiency characteristics were presented through theoretical analysis. Experimental results showed that the trend matched the analytical results, validating the theoretical analysis. Furthermore, using the analytical method in this paper, the proposed converter was compared with a DAB converter with the same symmetry as the three-phase transformer. As a result, the proposed converter can operate with higher efficiency over a wide range, indicating the effectiveness of selecting the operating modes depending on the voltage ratio and load.

Furthermore, the efficiency drop at medium loads is at most 1.25% points, indicating that the increase in power losses for specific phases due to asymmetry is small. Additionally, this efficiency drop is expected to be further minimized by optimizing the power devices, the size of magnetic cores, and winding thicknesses for each phase. Future challenges include establishing a soft start, seamless mode transition methods, and developing control strategies that optimize operating modes based on the output power and input-output voltage ratio.

REFERENCES

[1] R. De Doncker, D. Divan, and M. Kheraluwala, "A three-phase soft-switched high-power-density DC/DC converter for high-power applications," *IEEE Trans. Ind. Appl.*, vol. 27, no. 1, pp. 63–73, Jan./Feb. 1991.

[2] M. Kheraluwala, R. Gascoigne, D. Divan, and E. Baumann, "Performance characterization of a high-power dual active bridge DC-to-DC converter," *IEEE Trans. Ind. Appl.*, vol. 28, no. 6, pp. 1294–1301, Nov./Dec. 1992.

[3] H. Bai and C. Mi, "Eliminate reactive power and increase system efficiency of isolated bidirectional dual-active-bridge DC–DC converters using novel dual-phase-shift control," *IEEE Trans. Power Electron.*, vol. 23, no. 6, pp. 2905–2914, Nov. 2008.

[4] B. Zhao, Q. Song, and W. Liu, "Efficiency characterization and optimization of isolated bidirectional DC–DC converter based on dual-phase-shift control for DC distribution application," *IEEE Trans. Power Electron.*, vol. 28, no. 4, pp. 1711–1727, Apr. 2013.

[5] X. Liu et al., "Novel dual-phase-shift control with bidirectional inner phase shifts for a dual-active-bridge converter having low surge current and stable power control," *IEEE Trans. Power Electron.*, vol. 32, no. 5, pp. 4095–4106, May 2017.

[6] G. G. Oggier, G. O. García, and A. R. Oliva, "Switching control strategy to minimize dual active bridge converter losses," *IEEE Trans. Power Electron.*, vol. 24, no. 7, pp. 1826–1838, Jul. 2009.

[7] A. K. Jain and R. Ayyanar, "PWM control of dual active bridge: Comprehensive analysis and experimental verification," *IEEE Trans. Power Electron.*, vol. 26, no. 4, pp. 1215–1227, Apr. 2011.

[8] F. Krismer and J. W. Kolar, "Closed form solution for minimum conduction loss modulation of DAB converters," *IEEE Trans. Power Electron.*, vol. 27, no. 1, pp. 174–188, Jan. 2012.

[9] F. Krismer and J. W. Kolar, "Efficiency-optimized high-current dual active bridge converter for automotive applications," *IEEE Trans. Ind. Electron.*, vol. 59, no. 7, pp. 2745–2760, Jul. 2012.

[10] Y. A. Harrye, K. Ahmed, G. Adam, and A. Aboushady, "Comprehensive steady state analysis of bidirectional dual active bridge DC/DC converter using triple phase shift control," in *Proc. IEEE 23rd Int. Symp. Ind. Electron.*, 2014, pp. 437–442.

[11] A. Tong, L. Hang, G. Li, X. Jiang, and S. Gao, "Modeling and analysis of a dual-active-bridge-isolated bidirectional DC/DC converter to minimize RMS current with whole operating range," *IEEE Trans. Power Electron.*, vol. 33, no. 6, pp. 5302–5316, Jun. 2018.

[12] N. Hou and Y. W. Li, "Overview and comparison of modulation and control strategies for a nonresonant single-phase dual-active-bridge DC–DC converter," *IEEE Trans. Power Electron.*, vol. 35, no. 3, pp. 3148–3172, Mar. 2020.

[13] H. Zhou and A. M. Khambadkone, "Hybrid modulation for dual-active-bridge bidirectional converter with extended power range for ultracapacitor application," *IEEE Trans. Ind. Appl.*, vol. 45, no. 4, pp. 1434–1442, Jul./Aug. 2009.

[14] Z. Zhang, Y.-Y. Cai, Y. Zhang, D.-J. Gu, and Y.-F. Liu, "A distributed architecture based on microbank modules with self-reconfiguration control to improve the energy efficiency in the battery energy storage system," *IEEE Trans. Power Electron.*, vol. 31, no. 1, pp. 304–317, Jan. 2016.

[15] H. Akagi, T. Yamagishi, N. M. L. Tan, S.-i. Kinouchi, Y. Miyazaki, and M. Koyama, "Power-loss breakdown of a 750-v, 100-kw, 20-khz bidirectional isolated DC-DC converter using sic-mosfet/sbd dual modules," in *Proc. Int. Power Electron. Conf.*, 2014, pp. 750–757.

[16] L. Jin, B. Liu, and S. Duan, "ZVS operation range analysis of three-level dual active bridge DC-DC converter with phase-shift control," in *Proc. IEEE Appl. Power Electron. Conf. Expo.*, 2017, pp. 362–366.

[17] P. Liu, C. Chen, S. Duan, and W. Zhu, "Dual phase-shifted modulation strategy for the three-level dual active bridge DC–DC converter," *IEEE Trans. Ind. Electron.*, vol. 64, no. 10, pp. 7819–7830, Oct. 2017.

[18] H. Hayate, S. Shunsuke, K. Keisuke, and I. Junichi, "Development of T-type dual active bridge DC–DC converter with switching operation mode over wide-voltage-operation range," *IEEJ Trans. Ind. Appl.*, vol. 139, no. 4, pp. 388–400, 2019 (in Japanese).

[19] G. Xu, D. Sha, Y. Xu, and X. Liao, "Hybrid-bridge-based DAB converter with voltage match control for wide voltage conversion gain application," *IEEE Trans. Power Electron.*, vol. 33, no. 2, pp. 1378–1388, Feb. 2018.

[20] Y. P. Chan, M. Yaqoob, C. S. Wong, and K. H. Loo, "Realization of high-efficiency dual-active-bridge converter with reconfigurable multilevel modulation scheme," *IEEE Trans. Emerg. Sel. Topics Power Electron.*, vol. 8, no. 2, pp. 1178–1192, Jun. 2020.

[21] Z. Qin, Y. Shen, P. C. Loh, H. Wang, and F. Blaabjerg, "A dual active bridge converter with an extended high-efficiency range by DC blocking capacitor voltage control," *IEEE Trans. Power Electron.*, vol. 33, no. 7, pp. 5949–5966, Jul. 2018.

[22] T. Yutaro and H. Hitoshi, "Improvement of light-load efficiency by using a six-arm converter with series-parallel switching," *IEEJ Trans. Ind. Appl.*, vol. 140, no. 8, pp. 580–588, 2020 (in Japanese).

[23] A. Jafari, M. S. Nikoo, F. Karakaya, and E. Matioli, "Enhanced DAB for efficiency preservation using adjustable-tap high-frequency transformer," *IEEE Trans. Power Electron.*, vol. 35, no. 7, pp. 6673–6677, Jul. 2020.

[24] H. van Hoek, M. Neubert, and R. W. De Doncker, "Enhanced modulation strategy for a three-phase dual active bridge–boosting efficiency of an electric vehicle converter," *IEEE Trans. Power Electron.*, vol. 28, no. 12, pp. 5499–5507, Dec. 2013.

[25] J. Hu, N. Soltau, and R. W. De Doncker, "Asymmetrical duty-cycle control of three-phase dual-active bridge converter for soft-switching range extension," in *Proc. IEEE Energy Convers. Congr. Expo.*, 2016, pp. 1–8.
[26] F. Peng, H. Li, G.-J. Su, and J. Lawler, "A new ZVS bidirectional DC-DC converter for fuel cell and battery application," *IEEE Trans. Power Electron.*, vol. 19, no. 1, pp. 54–65, Jan. 2004.
[27] F. Krismer and J. W. Kolar, "Accurate power loss model derivation of a high-current dual active bridge converter for an automotive application," *IEEE Trans. Ind. Electron.*, vol. 57, no. 3, pp. 881–891, Mar. 2010.
[28] R. Haneda and H. Akagi, "Power-loss characterization and reduction of the 750-V 100-kw 16-kHz dual-active-bridge converter with buck and boost mode," *IEEE Trans. Ind. Appl.*, vol. 58, no. 1, pp. 541–553, Jan./Feb. 2022.

YIYU CHEN (Student Member, IEEE) received a B.S. degree in electrical engineering in 2022 from the Department of Electrical Engineering, Tokyo University of Science, Tokyo, Japan, where he is currently working toward the M.S. degree with the Faculty of Science and Technology, Department of Electrical Engineering. His research focuses on DC–DC converters.

RYOSUKE OTA (Member, IEEE) received the B.S., M.S., and Ph.D. degrees in electrical engineering from the Tokyo University of Science, Tokyo, Japan, in 2014, 2016, and 2019, respectively. From 2016 to 2018, he was with Inc. KADOKAWA, as a Novel Editor. From 2018 to 2020, he was also a Research Fellow with the Japan Society for the Promotion of Science (JSPS). In 2019 and 2020, he was a Visiting Researcher with The University of Auckland, Auckland, New Zealand. From 2020 to 2023, he was an Assistant Professor with the Tokyo University of Science. He is currently an Assistant Professor with Tokyo Metropolitan University, Hachioji, Japan. His research interests include power electronics, wireless power transfer, and DC-DC converters, among others. He was the recipient of the 2022 IEEJ Industry Applications Society Distinguished Transaction Paper Award, 2022 IEEJ Industry Applications Society Excellent Presentation Award, 2020 IEEE PELS WoW Best Paper Award, 2020 Young Engineer Presentation Award from IEICE, 2014 IEEJ Industry Applications Society Excellent Presentation Award, and 17th ICEMS Best Paper Award in 2014 from IEEE. He is also the Member of the IEEJ and IEICE.

NOBUKAZU HOSHI (Senior Member, IEEE) received the B.S., M.S., and Ph.D. degree in electrical engineering from the Department of Electrical Engineering, Yokohama National University, Yokohama, Japan. In 1997, he joined the Department of Electrical and Electronic Engineering, Ibaraki University, Hitachi, Japan, as a Research Associate and became an Assistant Professor in 2005. From 2008 to 2014, he was an Associate Professor and is currently a Professor with the Department of Electrical Engineering, Faculty of Science and Technology, Tokyo University of Science, Noda, Japan. His research interests include power electronics, motor control, electric vehicles, and hydrogen generation systems. He was a co-recipient of IEEE IAS Committee Prize Paper Award in 1998 and 2010, and the IEEJ Industry Applications Society Transactions Paper Award in 2013 and 2023.